remote sensing

MDPI

Article

Object-Oriented Remote Sensing Approaches for the Detection of Terrestrial Impact Craters as a Reconnaissance Survey

Habimana Emmanuel [1,2], Jaehyung Yu [1,3,*], Lei Wang [4], Sung Hi Choi [1,3] and Digne Edmond Rwabuhungu Rwatangabo [2]

1 Department of Astronomy, Space Science and Geology, Chungnam National University, Daejeon 34134, Republic of Korea; habimana838@gmail.com (H.E.); chois@cnu.ac.kr (S.H.C.)
2 School of Mining and Geology, University of Rwanda, Kigali 3900, Rwanda; drwabuhu@gmail.com
3 Department of Geological Sciences, Chungnam National University, Daejeon 31134, Republic of Korea
4 Department of Geography & Anthropology, Louisiana State University, Baton Rouge, LA 70803, USA; leiwang@lsu.edu
* Correspondence: jaeyu@cnu.ac.kr; Tel.: +82-42-821-6426

Abstract: The purpose of this study is to employ a remote sensing reconnaissance survey based on optimal segmentation parameters and an object-oriented random forest approach to the identification of possible terrestrial impact craters from the global 30-m resolution SRTM DEM. A dataset consisting of 94 confirmed and well-preserved terrestrial impact craters, 104 volcanic calderas, and 124 valleys were extracted from real-world surface features. For craters with different sizes, eight optimal scale parameters from 80 to 3000 have been identified using multi-resolution segmentation, where the scale parameters have a positive correlation (R^2 = 0.78) with the diameters of craters. The object-oriented random forest approach classified the tested impact craters, volcanic calderas, and valleys with an overall accuracy of 88.4% and a Kappa coefficient of 0.8. The investigated terrestrial impact craters, in general, have relatively lower rim circularity, higher length-to-width ratio, and lower relief, slope, and elevation than volcanic calderas. The topographic characteristics can be explained by geological processes associated with the formation and post-deformation of impact craters. The excavation and ejection by initial impact and rebound of excavated materials contribute to low elevation. The post-impact deformation, including inward collapse and slump of unstable rims, weathering, erosion, and sediment deposition, further reduces elevation and relief and modifies shapes resulting in lower circularity and higher length-to-width ratio. Due to the resolution limitation of the source DEM data and the number of real-world samples, the model has only been validated for craters of 0.88 to 100 km in diameter, which can be generalized to explore undiscovered terrestrial impact craters using cloud computing with global datasets provided by platforms such as Google Earth Engine and Microsoft Planetary Computer.

Keywords: impact craters; scale parameters; multi-resolution segmentation

check for updates

Citation: Emmanuel, H.; Yu, J.; Wang, L.; Choi, S.H.; Rwatangabo, D.E.R. Object-Oriented Remote Sensing Approaches for the Detection of Terrestrial Impact Craters as a Reconnaissance Survey. *Remote Sens.* **2023**, *15*, 3807. https://doi.org/10.3390/rs15153807

Academic Editors: Manuel Ángel Aguilar, Gino Dardanelli and Weiming Cheng

Received: 11 June 2023
Revised: 21 July 2023
Accepted: 27 July 2023
Published: 31 July 2023

1. Introduction

Impact craters are important geological features in planetary sciences formed by comets or asteroids colliding with the planetary surface [1]. The circular or sub-circular topographic feature represents the energy level of the meteorite impact, which can be observed by satellites [2]. Impact craters have been one of the major scientific focuses in the science community because they provide evidence for inference of planet of evolution and understanding of space materials [3]. Moreover, they are a critical indicator related to space hazards inducing secondary earthquakes and tsunamis [4]. Estimating impact crater ages assist in quantifying impact flux in the geological time scale and relates to other geological events in Earth's history [5]. Therefore, geoscientists have made substantial endeavors to detect and describe impact crater landscapes based on various sources such as remote sensing, geophysics, and geological data.

The number of confirmed craters is biased by the disparity in survey technology because most confirmed craters are located in developed countries [6]. Kenkmann et al. [7] reported 198 confirmed and 10 suspected impact craters unevenly distributed worldwide, with 65 in North America, 54 in Europe, 31 in Australia, 23 in Asia, 21 in Africa, and 14 in South America [7]. The regional differences indicate that the number of impact craters in developing countries should be higher than the current reports, and more cases could be identified in those low-finding areas.

Identification of terrestrial impact craters usually requires two major steps. The first step is the preliminary identification of crater candidates through remote sensing, including topographic, optical, gravity, or magnetic surveys, and the second step is a conclusive investigation by intensive geological surveys, including well-logging, lab analysis, geochemical analysis, and shock metamorphic experiments. These confirm the impact craters with ultimate evidence (shatter cones and planar deformation features, etc.) [8–10]. Remote sensing can provide worldwide coverage of preliminary assessment of possible crater locations to narrow down candidates using satellite data [11,12]. In addition, geophysical surveys play a major role in the identification of deeply eroded or buried suspected impact structures [13,14].

The topographic features from Digital Elevation Models (DEMs) can be used to identify possible candidates based on geomorphological characteristics such as crater rims and ring structures [9,15]. DEMs also can be used to define geomorphological parameters of confirmed caters from sophisticated geological surveys [16–18]. Additionally, the drainage networks associated with impact structures are also analyzed to trace the extent of the drainage basin [15]. The drainage network within a preserved impact crater shows drainage patterns such as centripetal or centrifugal radial drainage and sometimes concentric drainage where crater rims act as catchment [7,15].

Multispectral satellite data have been used to derive structure features and lithological discontinuities that might be related to impact cratering [11,15]. Linear features extracted from Landsat satellite data revealed the orientation of linear geological structures and distribution of lithological units, such as ejecta of brecciated materials and shock-induced alterations [15,19]. Radial and annular lineament patterns have been observed in several exposed impact structures as a result of concentric depressions and rim escarpments [9].

Furthermore, automatic computer algorithms have been used to detect impact craters based on the circular morphometric resemblance of impact structures displayed in remote sensing data [20]. Various Crater Detection Algorithms (CDAs) have been used on extraterrestrial impact craters such as lunar and Mars craters [21,22]. However, limited attempts have been made for the automatic detection of terrestrial craters [23]. Masaitis et al. [24] and Kenkmann et al. [7] highlighted that complex geological processes and size variations of terrestrial impact craters would hinder the automatic detection of terrestrial impact craters. Li et al. [25] also reported a challenge in distinguishing impact craters, volcanos, and valleys in deep learning for automatic crater detection because they share similar characteristics to the natural image.

The three types of impact crater, simple crater, complex crater, and impact crater basin, have distinctive topographic characteristics [2]. Typical fresh, simple impact craters have bowl-shaped depressions with a diameter of around 2 km for those formed in sedimentary rocks and about 4 km for crystalline rocks [8,26]. Fresh, complex impact craters also occur as circular or sub-circular topographic features with fresh central uplift peaks or concentric peak rings and a diameter greater than about 4 km. In addition, complex craters have a smaller depth-to-diameter ratio than simple craters [27,28]. Fresh impact crater basins have a relatively flat floor with one or more discrete terraces and the absence of sharp bowl-shaped topography and central uplift [28]. The impact basins have a diameter ranging from 3 km to 10 km [7].

Previous studies on the detection of impact craters using remote sensing have been focused on extraterrestrial impact craters, with few studies on terrestrial impact craters. This study aims to provide a reconnaissance survey method for the identification of possible terrestrial impact craters from global datasets. In view of the geometric characteristics of impact craters, DEMs can provide quantification of the geometric variables and, therefore, are the ideal data sources for reconnaissance surveys. For model development, this study collected 94 confirmed and well-preserved impact craters worldwide. Then, based on object attributes, a machine learning algorithm was tested for the classification of terrestrial impact craters from similarly shaped topography and commonly found land features such as volcanic calderas and valleys. The most important variables for differentiating impact craters from other terrestrial topographic features were identified using the machine learning algorithm. We expect this approach could contribute to the discovery of new impact craters with well-preserved topography.

2. Materials and Methods

To determine the optimal segmentation parameters for the detection of the exposed impact craters, the study investigated 94 confirmed exposed impact craters, including 24 simple, 66 complex, and 4 impact crater basins (~45% worldwide craters). The exposed impact craters can be defined as impact craters with a clear and easy-to-recognize circular morphology [7]. After the derivation of optimal segmentation parameters to define impact crater objects, object-based classification was carried out to test the detection of impact craters. In general, the morphology of impact craters can be defined as a circular depression bordered by an upraised rim formed by concentric normal faults and rebound of ejected materials [29]. We selected volcanic calderas to test classification efficiency with regard to features with similar topography. Volcanic calderas have circular depressions bordered by concentric or ring faults formed by the subsidence of the roof of the magma chamber due to the withdrawal of magma [30]. The ring faults of calderas exhibit geometrical properties similar to impact craters, such as diameter, topographic depression, and circular shape [31]. Therefore, this study included 104 volcanic calderas (44 single-pit and 60 coalesced-pit calderas) distributed over the world to test the detection efficiency of impact craters from similar topographic features (Figure 1, Appendix A, Table A2). Single-pit calderas are generally recognized by a single large depression, while coalesced-pit calderas are recognized by multiple interconnected depressions within a broader area [32–34]. This study also included valleys as an additional class for the classification model, which are common features associated with mountainous areas. We included 124 valleys to test the common features that can interfere with the detection of impact craters. The valleys have relatively shallow and wide depressions with gentle slope landforms, where the composite of valleys can form watersheds with various forms, such as fan or half-circle shapes [35,36].

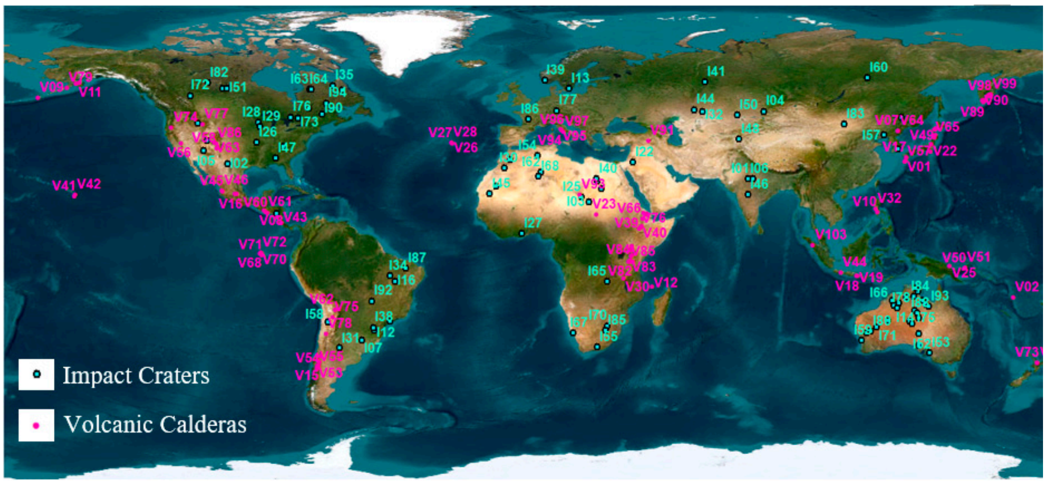

Figure 1. World map with the exposed impact craters and a sample of volcanic calderas locations.

2.1. Data Acquisition and Preparation

This study used the global Digital Elevation Model of Shuttle Radar Topography Mission data (SRTM DEM). DEM data with a resolution of 1 arcsec (~30 m/pixel) were downloaded from the USA Geological Survey (USGS) [37]. We used 94 confirmed impact craters because of the limited exposure of buried craters and the limited data coverage of the SRTM data [7] (Appendix A, Table A1). The buried impact craters are characterized by a lack of circular morphological expression on Earth's surface due to post-impact geological activities such as weathering and erosion [2]. Additionally, 104 volcanic calderas with diameter sizes analogous to those of impact craters were selected from the Collapse Caldera Worldwide Database to test the detection models [38] (Figure 1, Appendix A, Figure A1). Moreover, 124 valley objects that are commonly found in mountainous areas were randomly selected during the segmentation and used for object-oriented classification to assess the detection efficiency of impact craters.

The original SRTM DEMs were filled to remove void pixels, and then the impact craters and volcanic calderas were clipped to generate a mosaic image including all target impact craters and other types of topographic features (Figure 2). The extent of the clipped area was approximately 3 times the apparent diameter size of target impact craters or calderas. Then, additional morphometric datasets, including slope, aspect, and hillshade layers, were derived from the DEM mosaic for object-oriented segmentation, following the findings from previous studies. These derivatives could enhance the circular topographic imprint of the rims that create a topographic contrast compared to the surrounding areas [20].

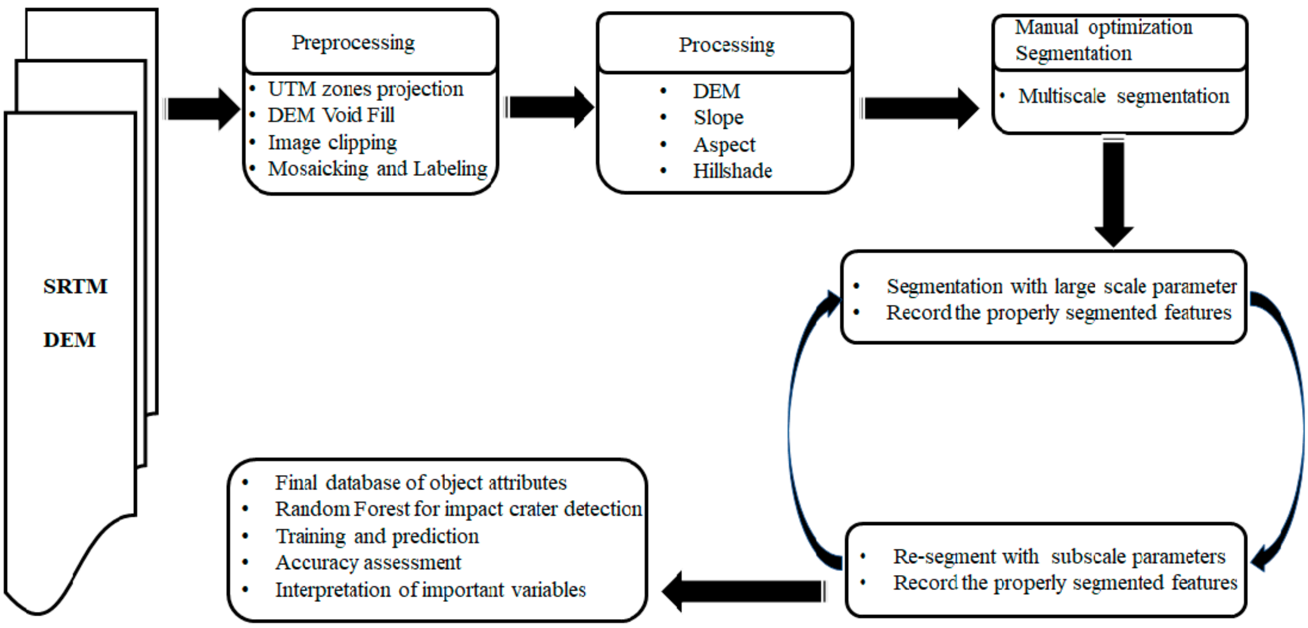

Figure 2. The graphical workflow for object-oriented terrestrial impact detection.

2.2. Optimum Scale Parameter Selection for Impact Crater Detection

In SRTM data, each crater consists of many 30-m pixels that define its geometries and topography. First, each crater should be extracted as an object with a clearly defined boundary. This study used a multi-resolution segmentation algorithm (MRS) implemented in eCognition developer 10.1 for the segmentation of the objects [39]. MRS employs a bottom-up region merging process of pixels. The segmentation starts by considering every pixel as a single object and accumulatively merging homogeneous pixels into distinct objects based on the scale parameter, shape and compactness, texture, and color. The merging process is stopped when the increase in homogeneity pixels exceeds the predefined scale in the eCognition software [20,40,41].

The segmentation results are mainly controlled by the Scale Parameter (SP) and associated shape and compactness [42], and, thus, different scale parameters would result in different sizes of segments. To determine the best scale parameters for optimal segmentation, the segmentation was iteratively conducted with changes in scale parameters from 5000 to 60 because of the size variability of impact craters and calderas (Figure 2). In this study, the shape of 0.4 and compactness of 0.6 were used for segmentation because they detected the circular rims effectively based on trial and error.

The topographical identification of the circumference of an impact crater is determined by the raised edge of the crater rim [7]. Based on this observation, we hypothesized that the circular topographic imprint of the rim on the DEM raster would induce the formation of homogeneous circular objects. Consequently, we employed a two-step assessment method to evaluate segmentation results. First, the segmentation results at each SP were subject to visual inspection to determine whether the segmentation was adequate to outline the impact crater rims. Then, the segmentation results that passed the inspection were used to calculate Area Fit Index (AFI). Area Fit Index (AFI) (Equation (1)) quantifies the fitness area between the reference area of impact craters (R) calculated from the Earth Impact Crater Database [2] and the area of impact crater object (S) derived from the segmentation.

$$AFI = \frac{area(R) - area(S)}{area(R)} \tag{1}$$

An AFI equal to 0 is an ideal segmentation, and AFI values ≤ 0.5 are considered a good agreement [43–46]. The number of properly segmented impact craters and AFI have been summarized for each SP, and the SPs with the most impact crater segmentation and the minimum AFI were selected as optimum scale parameters. The morphometric characteristics of impact craters segmented at each SP were analyzed to determine the relationship between SPs and morphometric parameters.

2.3. Random Forest Model for Terrestrial Impact Crater Detection

The objects segmented at optimal SPs for terrestrial impact craters were further used for the object-oriented classification model. As a result of segmentation, 70 objects of impact craters, 85 objects of volcanic calderas, and 124 objects of valleys were used to develop a random forest-based detection model (RF hereafter). A total of 16 attributes were extracted from segmented objects and used for the RF model (Table 1). Among the 16 attributes, 7 topographic attributes described the morphological variation of the landform, 3 geometric attributes quantified the shape, and 6 texture attributes described the surface structure or pattern based on Gray–Level Co-occurrence Matrix (GLCM) (Table 1). To avoid overfitting, multicollinearity analysis between the 16 variables was performed. Based on the analysis, 5 variables with high intercorrelation were removed, including Angular Second Moment (ASM), contrast, entropy, aspect, and standard deviation of elevation, and 11 variables with low intercorrelation coefficient (<0.6) were used for the RF classification model.

RF is a nonparametric machine learning algorithm based on randomly generated tree classifiers, and the classification is through the ensemble majority votes. In addition, important variables that effectively define the relationship between predictors and target features can be quantitatively derived by Mean Decrease Accuracy (MDA) and Mean Decrease Gini (MDG) scores [47]. The RF algorithm was implemented in the R software. A total of 30% of samples were randomly selected for validation, and Ntrees and Mtry are 500 and 3, respectively. The variable importance of impact crater detection was rated based on Mean Decrease Accuracy (MDA) and Mean Decrease Gini (MDG) scores to determine the major contributor of morphometric parameters for impact crater detection. The roles of major contributors were discussed on how those variables could be used for terrestrial impact crater detection.

Table 1. The attributes derived from detected objects.

Type	Parameters	Brief Description	References
Topographic	Elevation	Express the height of an object below or above sea level	[48]
	Slope	Express the steepness of the surface of an object	[49]
	Aspect	Express the orientation of slope of an object	[50]
	Hillshade	Illustrate the impression of the 3D surface of an object from the point of view of the sun	[50]
	Standard deviation of elevation	Express the variability of elevation within the object	[51]
	Standard deviation of slope	Express the variability of slope within the object	[51]
	Terrain Relief	Represent the difference between maximum and minimum elevation within the object	[52]
Geometric	Length/Width ratio	Represent the relative comparison between the length and width of an object	[48]
	Elliptical fit	Shape descriptor quantifies how much an area of an object fits the shape of an ellipse with a similar area	[48]
	Circularity	Shape descriptor that quantifies the roundness of an object: $(\text{Perimeter}^2)/(4\pi \times \text{Area})$	[53]
Texture (GLCM)	Homogeneity	Estimate the similarity between the pairs of pixels in the image object	[54]
	Dissimilarity	Estimate the difference between the pairs of pixels in the image object	
	Angular Second Moment (ASM)	Estimate the amount of homogeneity or uniformity within the image object	
	Contrast	Measure the local intensity variation in the image object	
	Correlation	Measure the linear dependency between the pairs of pixel values in the image object	
	Entropy	Measure the unpredictability or randomness of the relationship between the pixels in the image object	

3. Results and Discussion

3.1. Selection of Optimal Scale Parameter for Impact Crater Segmentation

The visual inspection for segmentation results at each SP from 5000 to 60 revealed that the SP and diameter of segmented impact craters have positive relationships where the larger SPs would segment larger impact craters. Moreover, we found that SPs larger than 2000 would segment impact craters with an approximate diameter $\geq$70 km, and SPs lower or equal to 2000 would segment impact craters with a diameter < 70 km.

The SPs from 2000 to 5000 segmented only one impact crater from 5 impact craters in the 70–180 km diameter range (Table 2). The properly segmented impact crater was the Manicouagan impact crater (Canada), with a visible ring of ~70 km diameter. The SP 3000 best-segmented the possible rim or ring, whereas SP 5000 and 4000 under-segmented and 2000 over-segmented the outer rims (Figure 3a). In addition, an AFI value of 0.45 for the SP 3000 confirmed the good performance of segmentation. The rim of some craters, such as the Vredefort crater in South Africa, have experienced erosion, causing the rim boundaries to become less distinct. Consequently, the segmentation process was unable to detect the evident rim boundary in such cases (Figure 3b). Large craters with diameters greater than 70 km are rare on Earth's surface and account for only about 5% of the samples. It might be attributed to Earth's atmosphere, geological activities, erosion, and plate tectonics compared to the other planets and the Moon [2,55]. Therefore, we recommend SP 3000 as the optimal segmentation parameter for craters larger than 70 km.

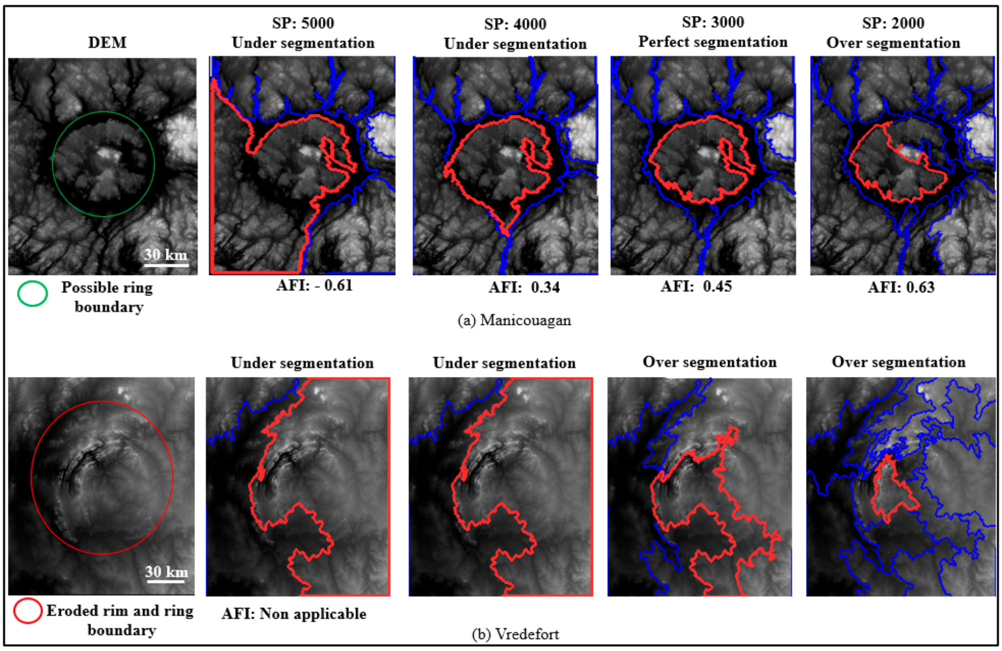

Figure 3. DEM layers of (**a**) Manicouagan impact crater (Canada); and (**b**) Vredefort crater (South Africa) with their respective multi scales segmentation results. Red segments represent the objects intended to suitably outline the possible crater rim at different SPs, and blue segments represent the various objects formed around other features.

Table 2. Attempted optimum scale parameters and number of detected features.

Segmentation Settings			Impact Craters			
SP	Shape	Compactness	Diameter Range (km)	Count Segmented (%)	AFI	Count Not Segmented (%)
5000–3000	0.4	0.6	70–180	1 (1.0)	0.48	2 (2.1)
2000	0.4	0.6	24–60	8 (8.5)	0.07–0.50	0
1000	0.4	0.6	8–39	12 (12.7)	0.01–0.41	0
700	0.4	0.6	6–30	6 (6.3)	0.08–0.43	2 (2.1)
400	0.4	0.6	6–17	9 (9.5)	0.04–0.43	3 (3.1)
200	0.4	0.6	1.8–12	21 (22.3)	0.08–0.49	6 (6.3)
100	0.4	0.6	1.8–6	6 (6.3)	0.12–0.44	0
80	0.4	0.6	0.88–3.4	7 (7.4)	0.12–0.35	1
60	0.4	0.6	0.024–0.64	0	0	10 (11.7)
	Overall:		70/94 (74.5%)			24 (25.5%)

Similarly, the segmentation results of the other SPs (2000, 1000, 700, 400, 200, 100, 80, 60) were evaluated, and the impact craters segmented from each SP varied because they vary in diameter and exposure level (Table 2, Figure 4). As a result, all SPs lower than 2000 except 60 have been selected as optimal scale parameters for impact crater segmentation. The diameter of segmented impact craters and 8 SPs showed a high correlation (R^2) of 0.78 (Figures 4 and 5).

The SP 200 properly segmented 21 out of 27 exposed impact craters with apparent diameters ranging from 1.8 to 12 km. The representative impact crater segmented by SP 200 is the Goat Paddock crater (Australia), 5 km in diameter (Figure 4). The highest detection in this scale was simply due to the large population of impact craters in the size range of terrestrial impact craters. Indeed, a previous study reported that almost half of terrestrial impact craters have a diameter range from 1 km to 10 km [7]. The smallest SP for impact crater segmentation was SP 80, which properly segmented 7 small-sized impact craters out of 8 with diameters in the range of 0.88–3.4 km. The scale mostly covered the smallest and most well-preserved simple impact craters, such as Tenoumer (Mauritania), Tswaing (South Africa), and Roter Kamm craters (Namibia). On the other hand, SP 60 over-segmented all 10 small impact craters of 0.024–0.64 km diameter. These small impact craters provided indiscernible topographic imprints from neighboring features on satellite data of 30 m resolution (Appendix A, Figure A2). Hence, SP 60 was not included as an optimal SP because it gave unreliable segmentation results for impact crater detection.

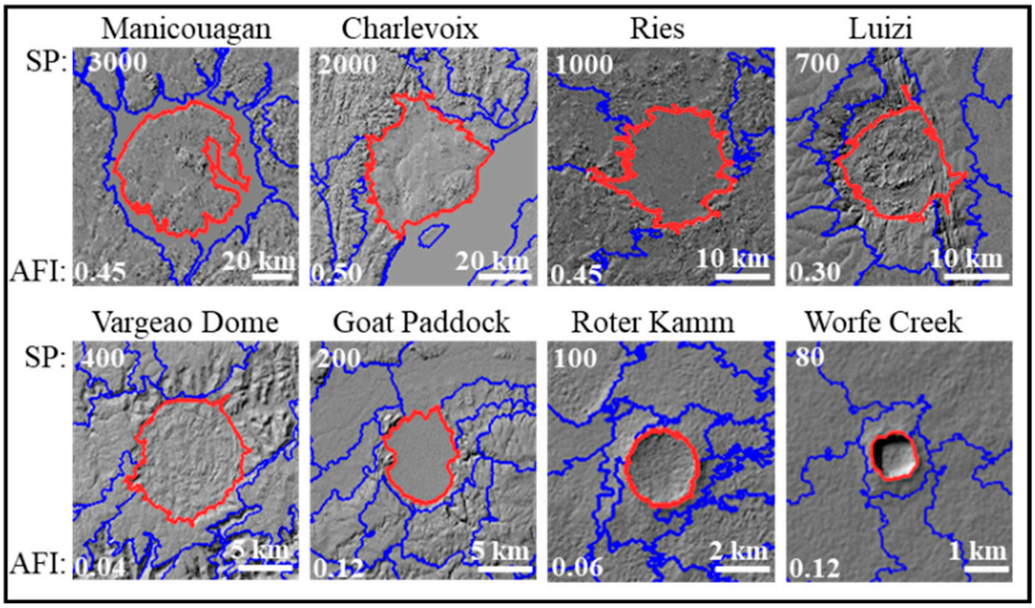

Figure 4. Multiple scale segmentation results of representative impact craters.

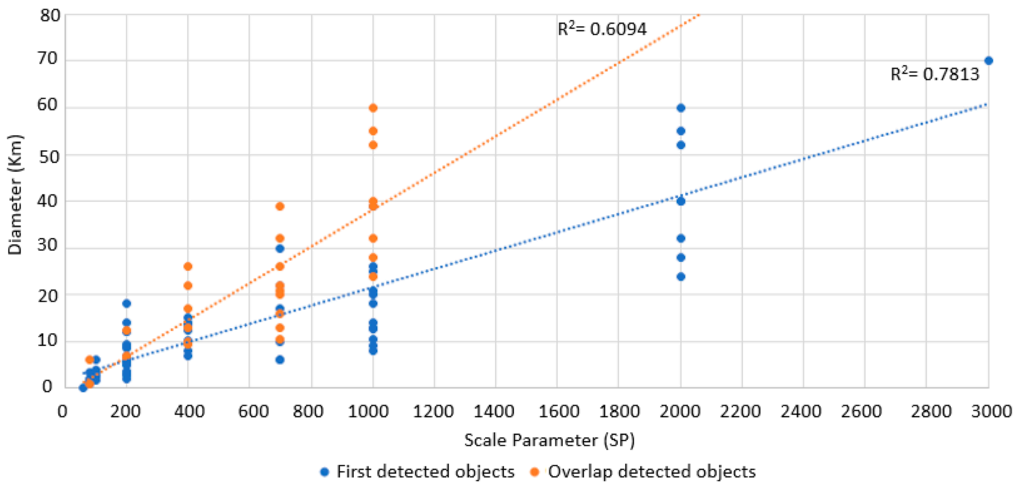

Figure 5. The overlapping situation for each scale impact craters; the blue dot points represent the impact craters that were firstly detected at larger SPs, and orange dot points represent the impact craters that were re-detected at other subscale scales.

In general, there was a large overlap in segmented impact craters between the neighboring SPs (Figure 5). As a result of visual inspection, 8/11 SPs (3000, 2000, 1000, 700, 400, 200, 100, 80) provided the optimum homogeneous circular objects around the rim of 70/94 (74.5%) impact craters. The circular segments formed for well-preserved craters like Rotter Kamm (Namibia) and Vargeão Dome (Brazil) showed nearly zero AFI, about 0.06 and 0.04 (Figure 4). However, the goodness of fit for moderately eroded impact craters such as Charlevoix (Canada) and Ries (Germany) was relatively high, about 0.5 and 0.45, respectively (Figure 4). On the other side, 24/94 (25.5%) impact craters were not segmented properly due to the complete destruction of circular topographic imprints regardless of diameter. The impact craters Rochechouart (23 km, France) and Kelly West (6.6 km, Australia) belong to this group.

3.2. RF Classification of Terrestrial Impact Craters and Other Topographic Features

The terrestrial impact craters segmented from optimal SPs were compared with similar topographic features such as volcanic calderas and commonly found topographic features like valleys based on the RF model. Similarly, segmentation was conducted for those topographic features, and as a result, a total of 85 properly segmented volcanic calderas and 124 valleys were used for RF classification. The object attributes of terrestrial impact craters and other topographic features were extracted and used for input values in RF classification (Table 1). A total of 70% of objects (70 impact craters, 85 volcanic calderas, and 124 valleys) were used for the calibration model, and the remaining 30% were used for validation. The accuracy assessment showed that the classification model showed very good performance, with an overall accuracy of 88.4% and a kappa coefficient of 0.82. Notably, the model separated impact craters and calderas from valleys very effectively with an accuracy close to 100% (Table 3).

Table 3. Confusion matrix of training, validation data from RF algorithm, where Production's Accuracy (PA) and User's Accuracy (UA) for each class are also presented.

		Training data			
Classes:	**Crater**	**Caldera**	**Valley**		
Crater	43	0	0	Accuracy	100%
Caldera	0	59	0	Kappa Coefficient	1
Valley	0	0	82		
		Validation data			
Classes:	**Crater**	**Caldera**	**Valley**	**PA (%)**	**UA (%)**
Crater	20	3	1	74.1	83.3
Caldera	7	23	0	88.5	76.6
Valley	0	0	41	97.6	100
		Overall accuracy			
Accuracy				88.4	
Kappa coefficient				0.82	

However, the accuracy for the detection of impact craters and volcanic calderas was relatively lower, with an accuracy of 74.1% and 88.5% due to the similarity in their topographic characteristics. Although the accuracy was the lowest for terrestrial impact craters, the accuracy of 78.7% is still considered good prediction accuracy, and thus, it infers that the remote sensing approaches to preliminary detection of undiscovered terrestrial impact craters can be effectively used.

The important variables for the detection of terrestrial impact craters were further derived from Mean Decrease Accuracy (MDA) and Mean Decrease Gini (MDG) indices (Figure 6). Based on the slope change shown by a sharp decrease in MDA and MDG, seven important variables were found: circularity, length-width ratio, relief, slope, elevation, homogeneity texture, and standard deviation of slope (Figure 6). Furthermore, violin plots visualized the distribution of the seven important variables of the three feature types based on kernel density estimation (Figure 7).

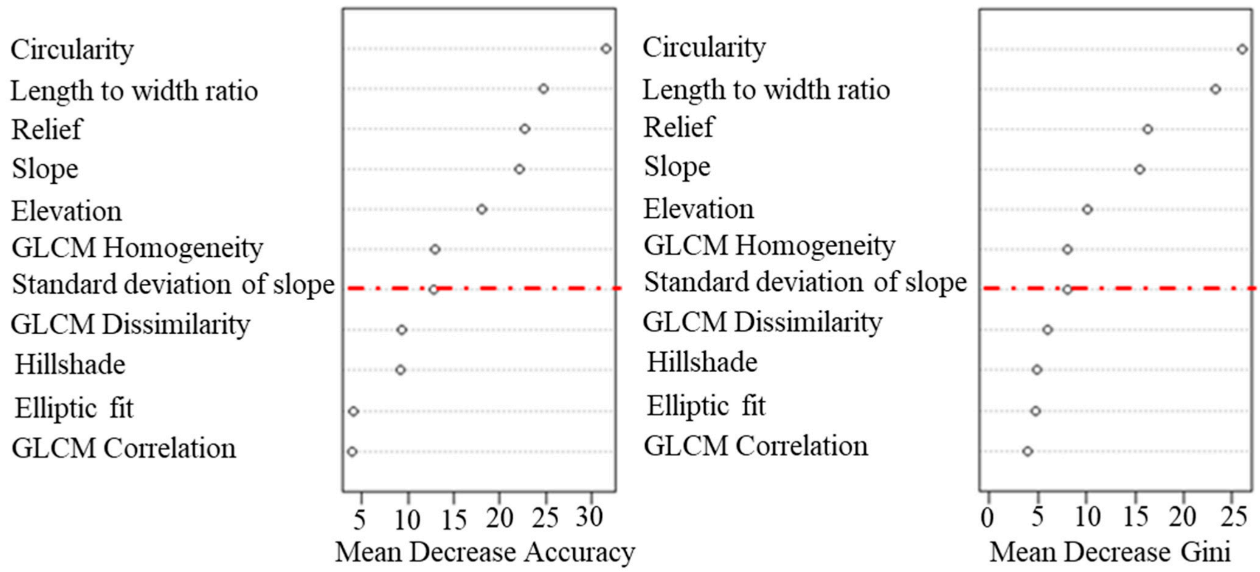

Figure 6. Variable importance of object attributes, the 7 variables above the red dotted line showed the major influence for detecting impact craters.

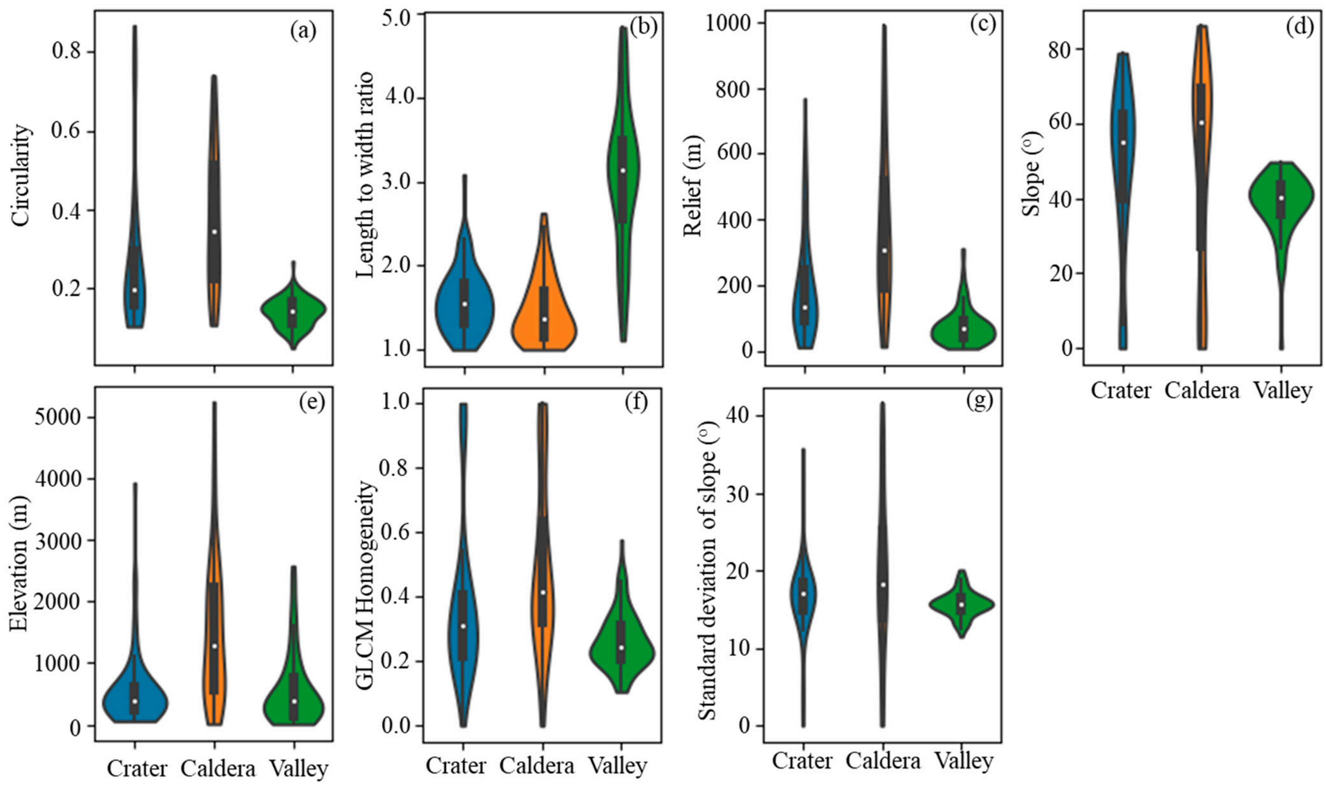

Figure 7. The violin plots for crater, caldera, and valley showing the density distribution of seven important variables: (**a**) Circularity index, (**b**) Lenth to width ratio index, (**c**) relief, (**d**) slope, (**e**) elevation, (**f**) GLCM Homogeneity and (**g**) standard deviation of slope.

The plots presented a significant difference in median locations and the shape of the violin plots between the classes. The white dot points mark the median of the data along with the interquartile range, and the bulge in shape indicates higher probability density. Among the three attribute groups, it was concluded that geometric attributes play the most important role in the detection of terrestrial impact craters, followed by topographic and surface texture attributes (Figures 6 and 7).

Circularity, a geometric attribute, was ranked as the most effective attribute for impact crater detection. Although both impact craters and volcanic calderas have circular shapes, they have differences in statistical distribution. For example, 75% of impact craters have circularity lower than 0.29, while 75% of volcanic calderas showed circularity higher than 0.22. A slight overlap was found in the range of 0.22–0.29 (Figure 7a). Meanwhile, valleys have distinctively lower circularity (Figure 7a). The circular shape of objects was further quantified by the length-to-width ratio. Half of the impact crater objects had a ratio higher than 1.5, and the majority of volcanic calderas (75%) were lower than 1.6. More than 75% of valleys showed a high ratio (>2.5) (Figure 7b).

In general, impact craters have jagged object boundaries, relatively lower circularity, and a higher length-to-width ratio compared to calderas. Indeed, prior studies reported that 34 impact craters have elliptical forms with a long-diameter axis to short-diameter axis ratio above 1.05 [7]. Moreover, oblique impactors, target heterogeneity, uneven erosion, and post-impact deformation have been presented as the main cause of elliptical form and modifications of the circular form of terrestrial impact crater rims [7]. The post-deformation processes include inward collapse and slump of rims, weathering, and erosion. Post-deformation modifies the shape of impact craters resulting in lower circularity and a high width-to-length ratio. The crater rims are composed of ejecta, melted, and brecciated materials, and thus, they are relatively vulnerable to erosion compared to crystalline igneous rocks. This phenomenon can also be confirmed by the ages of impact craters, which is related to exposed time for erosion and post-impact sedimentation in the central depression [56]. Indeed, impact crater objects with higher circularity (>0.72) were observed for 5 preserved simple impact craters, including Rotter Kamm, Worfe Creek, Meteor, Tenoumer, and Tswaing craters, which have ages of less than 5 Myrs [5]. In contrast, caldera rims have relatively higher circularity regardless of age because they are mainly formed by crystalline igneous rocks, which have higher resistance to erosion [57]. However, the circularity of caldera rims can be affected by characteristics of eruption, vents arrangement, and subsequent collapse. This study only used 104 volcanic calderas out of over 400 calderas worldwide [55,58]. Fully understanding the factors related to modification of the rim circularity needs more worldwide cases. Conversely, the valley objects were mostly characterized by elongated and asymmetrical shapes that could be associated with low circularity and a high length-to-width ratio.

Topographic attributes such as relief, slope, and elevation were also effective variables for differentiating terrestrial impact craters. The 75% of impact craters have relief less than 245 m, whereas 75% of volcanic calderas are higher than 192 m. The relief of valleys has a large overlap with impact craters, where 95% were lower than 192 m because they have similar depression (Figure 7c). The relatively lower relief of impact craters can be linked with shallow depression structures caused by ejecta and post-impact sediment deposition [10]. Indeed, Tsikals et al. [56] reported a decrease in relief of the central uplift ring and crater rims of 5 impact craters caused by sediment loading as a post-impact deformation. The shallower depression of impact craters was also found for lunar craters, which have a lower depth-to-diameter ratio [59]. On the other side, the relatively high internal relief found for volcanic calderas could be associated with a deep central depression formed by the collapse of the emptied magma chamber [60].

The slope attribute indicates that 75% of impact crater objects were mostly indicated by relatively gentle slopes less than 62°, while 50% of the volcanic caldera were mainly characterized by very steep rims with slopes greater than 60.2°. Valleys have distinctively low slopes of less than 49.6° (Figure 7d). Furthermore, a significant proportion of impact craters (88.5%) were found in elevations lower than 1000 m, while the majority (60%) of volcanic calderas are distributed in higher elevation ranges (1000–5233 m) (Figure 7e). The relatively lower elevation of impact craters can be explained by geological processes associated with the formation and post-deformation of impact craters. Impact craters are formed with circular rims formed by excavation and ejection, where the magnitude is controlled by the size and speed of the impacting object, the composition of the target material, and the angle of impact. This process induces relatively lower elevation than volcanoes, which create mountains. Moreover, the post-deformation of impact craters, such as collapse, slump of rims, and erosion, further reduces the elevation over time. The higher elevation of volcanic caldera can be explained by their topographic positioning, where most calderas are found in volcanic mountain summits that are relatively higher than most mountains. Volcanic calderas are mainly associated with magma eruption along tectonic boundaries, where most high mountain chains are distributed [61].

The GLCM homogeneity and standard deviation of slope showed a significant overlap for all three features compared to the other variables (Figure 7f,g). A substantial proportion (75%) of impact craters and volcanic calderas showed a homogeneity of less than 0.4 and 0.63, respectively. A relatively low homogeneity found for many impact craters could be the result of surface roughness caused by fractured, brecciated materials and central multi-structure rings [62]. Moreover, 75% of valleys were also characterized by homogeneity lower than 0.31 (Figure 7f). Similar patterns were also observed for the standard deviation of the slope variable, while volcanic calderas may have relatively higher variations in slope (Figure 7g).

4. Conclusions

This study is the first attempt to establish an optimal segmentation and object-oriented classification method based on confirmed and exposed terrestrial impact craters and DEM data. It confirmed that using remote sensing data, such as global digital elevation models, can effectively determine preliminary locations of undiscovered terrestrial impact craters around the world as a reconnaissance survey. Furthermore, this study not only tried to detect terrestrial impact craters but also detected volcanic calderas and tested the separability of other morphological features, such as valleys, from the impact craters. One limitation of our study is that the methods are only applicable to craters larger than 0.8 km in diameter. If smaller craters are to be detected, high-resolution DEMs are required, such as the TanDEM-X DEM by the German Aerospace Center. Moreover, this approach can only narrow down possible terrestrial impact crater candidates where topographic features are well-preserved. A more systematic geological analysis must follow up to validate the existence of terrestrial impact craters.

We introduced optimal scale parameters for the segmentation of terrestrial impact craters and detection of craters based on object-based attributes along with other terrestrial topographic features. The multi-resolution segmentation algorithm depicted the circular topographic imprints of impact craters and volcanic caldera rims from four morphometric layers derived from SRTM DEM data, including elevation, slope, aspect, and hillshade. Eight scale parameters ranging from 80 to 3000 were selected as the optimum scale parameters for terrestrial impact craters, which showed the goodness of fit area (0.01–0.5) and high correlation (R^2 = 0.78) with diameters in the range of 0.88–100 km. Given the fact that terrestrial impact craters with wide diameters (>100 km) are rarely found (<5%) because of high atmospheric pressure [2], SP of 3000 could be the optimal segmentation parameter for large terrestrial impact craters. The smallest impact craters (0.024–0.64 km) are vulnerable to surface erosion [11] and have indiscernible topographic imprints with 30 m resolution data. Hence, the segmentation threshold for terrestrial impact craters with SRTM DEM is a diameter of 0.88 km which could be segmented by SP of 80, which is the minimum scale parameter suggested by our analysis.

The object-oriented classification using Random Forest successfully detected terrestrial impact craters as well as volcanic calderas and valleys, showing an overall accuracy of 88.4% and a Kappa coefficient of 0.8. The detection accuracy of impact craters was the lowest, with 78.7% among the three topographic features. The relatively lower accuracy was associated with misclassification with volcanic caldera due to morphological similarity. The detection accuracy was highest for valleys (98.8%), followed by volcanic calderas (82.6%). Although the accuracy was lowest for terrestrial impact craters, the accuracy of 78.7% is still considered good prediction accuracy. This infers that this remote sensing approach to the preliminary detection of undiscovered terrestrial impact craters can be effectively used.

The important variables for the detection of terrestrial impact craters were identified as circularity, length-to-width ratio, relief, slope, and elevation. Terrestrial impact craters, in general, have relatively lower circularity and higher length-to-width ratios compared to volcanic calderas and significantly higher circularity and lower length-to-width ratios compared to valleys. Moreover, terrestrial impact craters have relatively lower relief, slope, and elevation than volcanic calderas and significantly higher relief, slope, and elevation than valleys. These geometric and topographic characteristics can be explained by geological processes associated with the formation and post-deformation of impact craters and volcanic calderas. The topography of impact craters surrounded by rims is formed by excavation and ejection and rebound and relaxation, and those processes induce relatively lower elevation. The post-deformation of impact craters, including inward collapse and slump of rims, post-impact erosion, and post-sediment deposition, lower the elevation, relief, and circularity with time. On the other hand, volcanic calderas are mostly associated with volcanic eruptions along tectonic boundaries where high mountain chains are distributed. Moreover, the deep central depression caused by the collapse of the emptied magma chamber results in relatively higher relief and slope. Compared to the impact crater rims, which are relatively unstable due to rapid excavation and the effects of the shock wave, the crystalline walls of volcanic calderas are more resistant to erosional processes, showing higher circularity and a lower width-to-length ratio. Moreover, the GLCM homogeneity of elevation could be included as a useful variable.

This study used 94 exposed and confirmed terrestrial impact craters (45% of worldwide impact craters) and incorporated similar topographic features, such as volcanic calderas, and the most common features, such as valleys. Given the fact that we have introduced a wide range of terrestrial impact craters from a diameter size of 0.88 to 100 km, the method can be generalized to the detection of unidentified craters worldwide using the global DEM models as a reconnaissance survey method. The segmentation parameters and detection variables introduced in this study could significantly contribute to the discovery of hidden terrestrial impact crater candidates in developing countries and remote areas.

Author Contributions: Methodology, H.E. and J.Y.; Software, H.E.; Validation, H.E.; Formal analysis, H.E. and J.Y.; Investigation, H.E. and J.Y.; Resources, J.Y.; Writing—original draft, H.E. and J.Y.; Writing—review & editing, J.Y. and L.W.; Visualization, H.E.; Supervision, J.Y. and D.E.R.R.; Project administration, J.Y. and S.H.C.; Funding acquisition, S.H.C. All authors have read and agreed to the published version of the manuscript.

Funding: This research was funded by [National Research Foundation of Korea] grant number [RS-2023-00208476] and [NRF-2021R1A4A5026233].

Conflicts of Interest: The authors declare no conflict of interest.

Appendix A

Table A1. The confirmed and exposed terrestrial impact craters used in this study were collected from an encyclopedic atlas of terrestrial impact craters [2,7].

Impact Crater	Country	Latitude	Longitude	ID	Diameter (km)	Exposure	Target Lithology	Type	Ages (ma)
Dhala	India	25.298	78.142	I01	12	ex, pc	Crystalline	C	1700–2500
Sierra Madera	USA	30.596	−102.912	I02	12	ex, pc	Sandstone	C	100
Gweni-Fada	Chad	17.421	21.755	I03	14–22	ex, pc	Sandstone	C	355
Bigach	Kazakhstan	48.568	82.036	I04	8	ex, pc	Mixed	C	3–5
Meteor Crater	USA	35.027	−111.023	I05	1.2	ex, pc	Sandstone	S	0.05
Ramgarh	India	25.335	76.624	I06	10.2	ex, pc	Sandstone	C	165
Cerro do Jarao	Brazil	−30.211	−56.539	I07	13	ex, smor	Sandstone	C	137
Connolly Basin	Australia	−23.538	124.761	I08	9	ex, pc	Sandstone	C	55–75
Tenoumer	Mauritania	22.918	−10.405	I09	1.9	ex, pc	Mixed	S	1.52
Piccaninny	Australia	−17.420	128.438	I10	7	ex, smor	Sandstone	C	360

Table A1. *Cont.*

Impact Crater	Country	Latitude	Longitude	ID	Diameter (km)	Exposure	Target Lithology	Type	Ages (ma)
Chogye	SouthKorea	35.537	128.269	I11	7	ex, pc	Sandstone	C	0.03–0.06
Vargeao Dome	Brazil	−26.805	−52.164	I12	12.4	ex	Sandstone	C	137
Mien	Sweden	56.431	14.856	I13	9	ex, sub	Crystalline	C	118.7
Gow	Canada	56.453	−104.482	I15	5	ex, sub	Crystalline	C	250
Santa Marta	Brazil	−10.167	−45.233	I16	10	ex, pc	Sandstone	C	93
Acraman	Australia	−32.017	135.450	I17	40–85	ex, sub	Crystalline	C	580
Gosses Bluff	Australia	−23.817	132.308	I18	22	ex, pc	Sandstone	C	142
Upheaval Dome	USA	38.433	−109.928	I20	6	ex	Sandstone	C	66–100
Foelsche	Australia	−16.676	136.784	I21	6	ex, pc	Sandstone	C	541–981
Jebel Waqf as Suwwan	Jordan	31.039	36.807	I22	6.1	ex, pc	Sandstone	C	37
Agoudal	Morocco	31.996	−5.516	I24	2.8	ex	Sandstone	C	0.3
Aorounga	Chad	19.084	19.244	I25	12.6–16	ex	Sandstone	C	355
Decaturville	USA	37.890	−92.720	I26	6	ex, pc	Sandstone	C	300
Bosumtwi	Ghana	6.500	−1.408	I27	10.5	ex, sub	Mixed	C	1.07
Decorah	USA	43.300	−91.772	I29	5.6	pc	Sandstone	T	460–483
Ouarkziz	Algeria	29.004	−7.551	I30	3.5	ex, pc	Sandstone	T	66
Zhamanshin	Kazakhstan	48.350	60.937	I32	14	ex, pc	mixed	C	0.75–1.1
Oasis	Libya	24.572	24.412	I33	5.2–18	ex, pc	Sandstone	C	120
Serra da Cangalha	Brazil	−8.082	−46.857	I34	13.7	ex	Crystalline	C	300
La Moinerie	Canada	57.440	−66.586	I35	8	ex, sub	Crystalline	C	400
Middlesboro	USA	36.631	−83.728	I36	6	ex	Sandstone	C	290–300
Colonia	Brazil	−23.880	−46.706	I37	3.6	ex, pc	Crystalline	T	5–36
Vista-Alegre	Brazil	−25.961	−52.690	I38	9.5	ex	Mixed	C	111–134
B.P. structure	Libya	25.318	24.310	I40	3.4	ex	Sandstone	C	120
Ragozinka	Russia	58.706	61.797	I41	9	ex, pc	mixed	C	50
Goyder	Australia	−13.477	135.040	I43	3	ex, pc	Sandstone	C	150–1400
Chiyli	Kazakhstan	49.177	57.834	I44	5.5	ex, pc	Sandstone	C	5.5
Lonar	India	19.974	76.509	I46	1.88	ex, sub	Crystalline	S	0.57
Wetumpka	USA	32.525	−86.176	I47	7	ex	Crystalline	C	84
Karakul	Tajikistan	39.067	73.433	I48	52	ex, smor	Mixed	C	50–5
Pantasma	Nicaragua	13.365	−85.954	I49	14	ex	Crystalline	C	0.8
Shunak	Kazakhstan	47.207	72.761	I50	2.8	ex, pc	Crystalline	S	34
Deep Bay	Canada	56.415	−102.983	I51	13	ex, sub	Crystalline	C	95–102
Crawford	Australia	−34.728	139.033	I53	8.5	ex	Crystalline	C	32–38
Talemzane	Algeria	33.315	4.034	I54	1.75	ex, pc	Sandstone	S	0.5–3
Xiuyan	China	40.364	123.460	I57	1.8	ex, pc	Crystalline	S	0.05
Goat Paddock	Australia	−18.348	126.677	I61	5	ex, pc	Sandstone	T	56–64
Tin Bider	Algeria	27.600	5.112	I62	6	ex, pc	Sandstone	C	50
Clearwater West	Canada	56.211	−74.500	I63	32	ex, sub	Mixed	C	290–300
Clearwater East	Canada	56.064	−74.083	I64	24	ex, sub	Mixed	C	460–470
Spider	Australia	−16.742	126.089	I66	13	ex, smor	Sandstone	C	573
Roter Kamm	Namibia	−27.762	16.289	I67	2.5	ex, pc	Sandstone	S	5
Yilan	China	46.391	129.311	I69	1.85	ex, pc	Crystalline	S	0.05
Tswaing	SouthAfrica	−25.411	28.083	I70	1.13	ex, sub	Mixed	S	0.22
Shoemaker	Australia	−25.881	120.883	I71	30	ex, pc	Sandstone	C	1630
Brent	Canada	46.078	−78.482	I73	3.8	ex, pc	Crystalline	S	396–453
Ries	Germany	48.873	10.695	I77	26	ex, pc	Crystalline	C	15
Wolfe creek	Australia	−19.170	127.795	I78	0.88	ex, pc	Sandstone	S	0.12
Cleanskin	Australia	−18.170	137.942	I79	15	ex, pc	Sandstone	C	540–1400
Luizi	D.R. Congo	−10.175	28.006	I65	17	ex	Sandstone	C	575
Carswell	Canada	58.418	−109.517	I82	39	ex, smor	Mixed	C	481
Strangways	Australia	−15.200	133.567	I84	25–40	ex, pc	Mixed	C	646
Sao Miguel do Tapuio	Brazil	−5.617	−41.388	I87	21	ex	Sandstone	C	120
Amelia Creek	Australia	−20.858	134.883	I88	20	ex	Mixed	C	600–1600
Mistastin	Canada	55.891	−63.311	I89	28	ex, sub	Crystalline	C	36.6
Charlevoix	Canada	47.533	−70.350	I90	55	ex, sub	Mixed	C	450
Beaverhead	USA	44.600	−112.967	I91	60–75	ex, pc	Mixed	C	600
Araguainha	Brazil	−16.785	−52.983	I92	40	ex	Crystalline	C	252–259
Lawn Hill	Australia	−18.693	138.652	I93	20	ex, pc	Sandstone	C	472
Manicouagan	Canada	51.399	−68.683	I94	70–100	ex, sub	Crystalline	C	214
Liverpool	Australia	−12.393	134.047	I81	2	ex, pc	Sandstone	S	150
Tabun-Khara obo	Mongolia	44.131	109.654	I83	1.3	ex, pc	Sandstone	S	145–163
Ritland	Norway	59.249	6.422	I39	2.7	ex, pc	mixed	S	500–540
Aouelloul	Mauritania	20.241	−12.675	I45	0.39	ex, pc	Sandstone	S	3.1

Table A1. *Cont.*

Impact Crater	Country	Latitude	Longitude	ID	Diameter (km)	Exposure	Target Lithology	Type	Ages (ma)
Dalgaranga	Australia	−27.633	117.289	I56	0.024	ex, pc	Crystalline	S	0.27
Monturaqui	Chile	−23.928	−68.262	I58	0.36	ex	Crystalline	S	0.663
Kalkkop	SouthAfrica	−32.709	24.432	I55	0.64	ex, pc	Sandstone	S	0.25
Amguid	Algeria	26.088	4.395	I68	0.45	ex, pc	Sandstone	S	0.1
Kamil	Egypt	22.018	26.088	I19	0.045	ex	Sandstone	S	0.003
Boxhole	Australia	−22.613	135.196	I14	0.17	ex	Crystalline	S	0.017
Whitecourt	Canada	53.999	−115.596	I72	0.036	ex	Sandstone	S	0.001
Henbury	Australia	−24.571	133.148	I23	0.18	ex, pc	Sandstone	S	0.0042
Rio Cuarto	Argentina	−32.871	−64.183	I31	4.5	ex	Sandstone	S	0.11
Yallalie	Australia	−30.443	115.771	I59	12	pc	Sandstone	C	83.6–89.8
Presquile	Canada	49.726	−74.833	I74	22	ex, sub	Crystalline	C	500
Macha	Russia	60.085	117.652	I60	0.3	ex, pc,	Sandstone	C	0.0073
Rock Elm	USA	44.717	−92.228	I28	6.5	ex, pc	Sandstone	C	410–460
Mount Toondina	Australia	−27.945	135.359	I52	4	ex, pc	Sandstone	C	66–144
Kelly west	Australia	−19.933	133.950	I75	14	ex, pc	Sandstone	C	541
Matt Wilson	Australia	−15.506	131.181	I42	7.5	ex	Sandstone	C	1400–1500
Sudbury	Canada	46.600	−81.183	I76	180–200	ex, pc	Crystalline	C	1849
Vredefort	SouthAfrica	−27.009	27.500	I85	180–275	ex, pc	Crystalline	C	2023
Rochechouart	France	45.831	0.782	I86	23	ex	Crystalline	C	201
Yarrabubba	Australia	−27.183	118.833	I80	30	ex, pc	Sandstone	C	2246

C: Complex, S: Simple, T: Transitional, ex: exposed, pc: partial covered, smor: subdued morphology, sub: submerged.

Table A2. Volcanic calderas used in this study were selected from collapse caldera worldwide database (CCDB) [38].

Volcanic Calderas	Country	Latitude	Longitude	D_max	D_min	Type	ID
Toba	Indonesia	2.580	98.830	100	30	C	V103
Taal	Philippines	14.010	120.998	30	25	S	V10
Kawah Ijen	Indonesia	−8.119	114.056	20	20	S	V18
Ijen_II	Indonesia	−8.058	114.244	18	17	S	V19
Shikotsu	Japan	42.751	141.317	15	13	S	V49
Long Valley	USA	37.717	−118.884	32	18	C	V56
Solitario	USA	29.451	−103.809	16	16	C	V62
Rotorua	NewZeland	−38.080	176.250	20	16	S	V73
Crater Lake	USA	42.930	−122.113	10	8	S	V74
Henry’s Fork Caldera	USA	44.330	−111.330	37	29	C	V77
Ngorongoro	Tanzania	−3.177	35.580	19	16	S	V80
Kapenga	NewZeland	−38.089	176.273	?	?	C	V92
Colli Albani	Italy	41.754	12.700	12	10	C	V97
Copahue	Chile & Argentine	−37.858	−71.177	10	10	S	V03
Paektu Mountain	China & N. Korea	42.005	128.056	14	12	S	V07
Karymshina	Russia	54.118	159.657	25	15	C	V101
Aso	Japan	32.885	131.084	25	18	C	V17
Mount Longonot	Kenya	−1.155	36.354	12	8	C	V37
Valles	USA	35.870	−106.570	22	16	C	V58
Braciano	Italy	42.316	12.174	20	15	S	V96
Akademia Nauk	Russia	53.981	159.462	11	11	S	V98
Uzon	Russia	54.500	159.970	12	9	C	V99
Ayarza	Guatemala	14.420	−90.120	7	5	S	V08
Mount Okmok	USA	53.468	−168.175	9.3	9.3	C	V09
Deriba	Sudan	12.950	24.270	5	5	C	V23
Toya	Japan	42.598	140.856	10	9	C	V48
Mount Silali	Kenya	1.152	36.231	8	5	C	V59
Ilopango	El Salvador	13.670	−89.050	11	8	C	V60
Alcedo	Ecuador	−0.430	−91.120	7.4	6.1	S	V67
Mount Aniakchak	USA	56.864	−158.151	10	10	C	V79
Emi Koussi	Chad	19.851	18.538	16	12	C	V93
Huichapan	Mexico	20.340	−99.550	10	10	C	V104
Sollipulli	Chile	−38.970	−71.520	4	4	S	V15
Gadamsa	Ethiopia	8.356	39.181	7	9	C	V24
Karkar	New Guinea	−4.650	145.967	5.5	3.2	C	V25
Agua de Pau	Portugal	37.770	−25.470	7	4	S	V26
The Barrier	Kenya	2.320	36.587	6	5	C	V29

Table A2. *Cont.*

Volcanic Calderas	Country	Latitude	Longitude	D_max	D_min	Type	ID
Mallahle	Ethiopia	13.270	41.650	6	6	C	V34
Asavyo	Ethiopia	13.098	41.599	12	12	C	V35
Suswa	Kenya	−0.915	36.457	12	8	C	V36
Kone	Ethiopia	8.840	39.688	6	5	C	V40
San Pedro	Mexico	21.263	−104.698	8	8	C	V46
Gallosuelo	NewZeland	−5.200	151.240	?	?	S	V51
Darwin	Ecuador	−0.180	−91.280	5	5	S	V68
Cerro Azul	Ecuador	−0.170	−91.240	5	5	S	V69
Sierra Negra	Ecuador	−0.830	−91.170	10	7	S	V71
Worf	Ecuador	−0.020	−91.350	7	5	S	V72
Cerro Panizos	Argentina	−22.187	−66.681	15	15	C	V75
Gadamsa	Ethiopia	8.350	39.180	10	8	C	V76
Incapillo	Argentina	−27.902	−68.824	6	5	C	V78
Olmoti	Tanzania	−3.016	35.652	6.5	6.5	C	V82
Nemurt	Turkey	38.621	42.235	8.5	7	S	V91
Vico	Italy	42.120	12.230	-	-	C	V94
Montefiascone	Italy	42.579	11.931	3	3	S	V95
Laslajas	Nicaragua	12.300	−85.730	7	7	C	V04
Krasheninnikov	Russia	54.593	160.273	11	9	C	V102
Karthala	Comores Island	−11.760	43.353	4	3	S	V12
Ale Bagu	Ethiopia	13.508	40.632	3	2.1	C	V13
Amealco	Mexico	20.126	−100.169	11	11	C	V16
Numazawa	Japan	37.450	139.579	3	2	C	V22
Sete Cidades	Portugal	37.870	−25.780	5	5	S	V28
Fantale	Ethiopia	8.984	39.907	4	3	S	V39
Mauna Loa	USA	19.479	−155.603	6.2	2.5	C	V41
Fernandina	Ecuador	−0.370	−91.550	6.5	6.5	S	V70
Embagai	Tanzania	−2.911	35.827	4	4	S	V81
Gorely Khrebet	Russia	52.558	158.027	13	10	C	V87
Changbaishan	China & N. Korea	42.005	128.058	5	5	S	V05
Mount Katmai	USA	58.260	−154.975	10	10	S	V11
Towada IV	Japan	40.500	140.900	3.5	3	S	V21
Furnas	Portugal	37.770	−25.320	6	6	C	V27
Kaguyak	USA	58.613	−154.053	3	2.5	S	V31
Mazama	USA	58.613	−154.053	10	8	C	V38
Villarrica	Chile &Argentine	−39.420	−71.950	9	6	C	V53
Aoba (Ambae)	Vanuatu	−15.389	167.835	2.1	2.1	S	V02
Izu-Oshima	Japan	34.724	139.394	4.5	3.5	C	V06
Ngozi	Tanzania	−9.010	33.554	3	3	S	V30
Pinatubo	Philippines	15.142	120.350	2.5	2.5	S	V32
Cerro Azul	Chile	−35.653	−70.761	4	5	S	V33
Geger Halang	Indonesia	−6.896	108.408	4	4	C	V44
Ceboruco	Mexico	21.125	−104.508	3.7	3.7	C	V45
Mount Meru	Tanzania	−3.247	36.748	3.5	3.5	C	V52
Ikeda	Japan	31.237	130.561	5	4	C	V57
Coate peque	El Salvador	13.859	−89.553	5	5	C	V61
TianChi	China	42.007	128.054	5	5	S	V64
Tazawa	Japan	39.721	140.663	6	6	S	V65
Sakurajima	Japan	31.578	130.661	23	17	C	V01
Conguillio	Chile	−38.901	−71.728	4	3	S	V14
Paka	Kenya	0.918	36.191	1.5	1.5	S	V20
Mauna Kea	USA	19.813	−155.472	4.2	2.5	C	V42
Poas	Costa Rica	10.200	−84.233	2.5	2.5	S	V43
Kuttara	Japan	42.500	141.180	3	3	S	V47
Gallosuelo	NewZeland	−5.342	151.117	13	10.5	C	V50
Logo Tromen	Chile-Argentine	−39.931	−72.028	5	6	C	V54
Mocho chosheunco	Chile-Argentine	−39.500	−71.715	5	4	C	V55
Lake City	USA	37.955	−107.391	18	15	C	V63
Groppo	Ethiopia	11.715	40.232	3.8	3.8	C	V66
Monduli	Tanzania	−2.868	35.949	2.9	2.9	S	V83
Gela	Tanzania	−2.763	35.916	3.1	3.1	S	V84
Oldeani	Tanzania	−3.297	35.449	3	3	S	V85
Creede	USA	37.748	−106.922	25	20	C	V86
Mutnovsky	Russia	52.451	158.166	9	9	C	V88
Ksudach	Russia	51.800	157.530	7	7	C	V89
Opala	Russia	52.543	157.339	14	12	C	V90
Mary Semyachik	Russia	54.058	159.442	10	10	C	V100

C: Coalesced pit, S: Single pit, D_min: Minimum diameter, D_max: Maximum diameter.

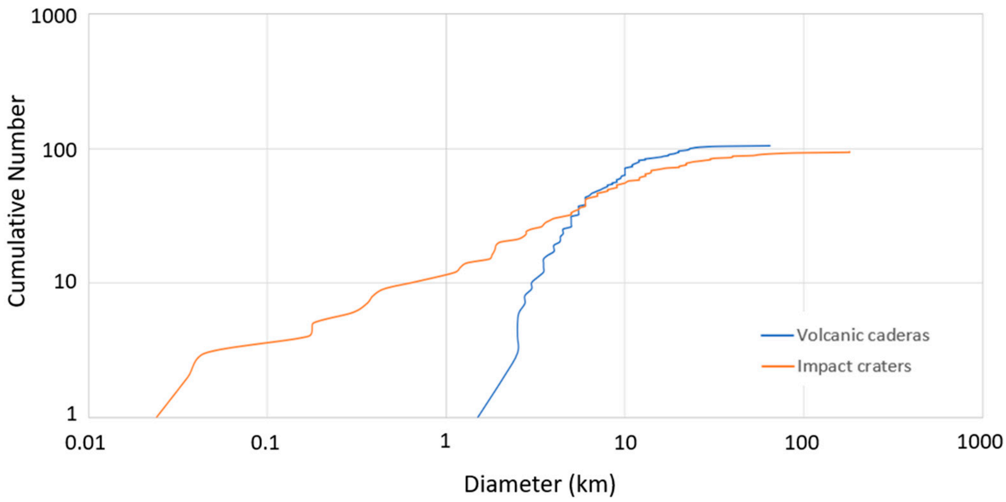

Figure A1. Size frequency distribution plot of impact craters and volcanic calderas used in this study.

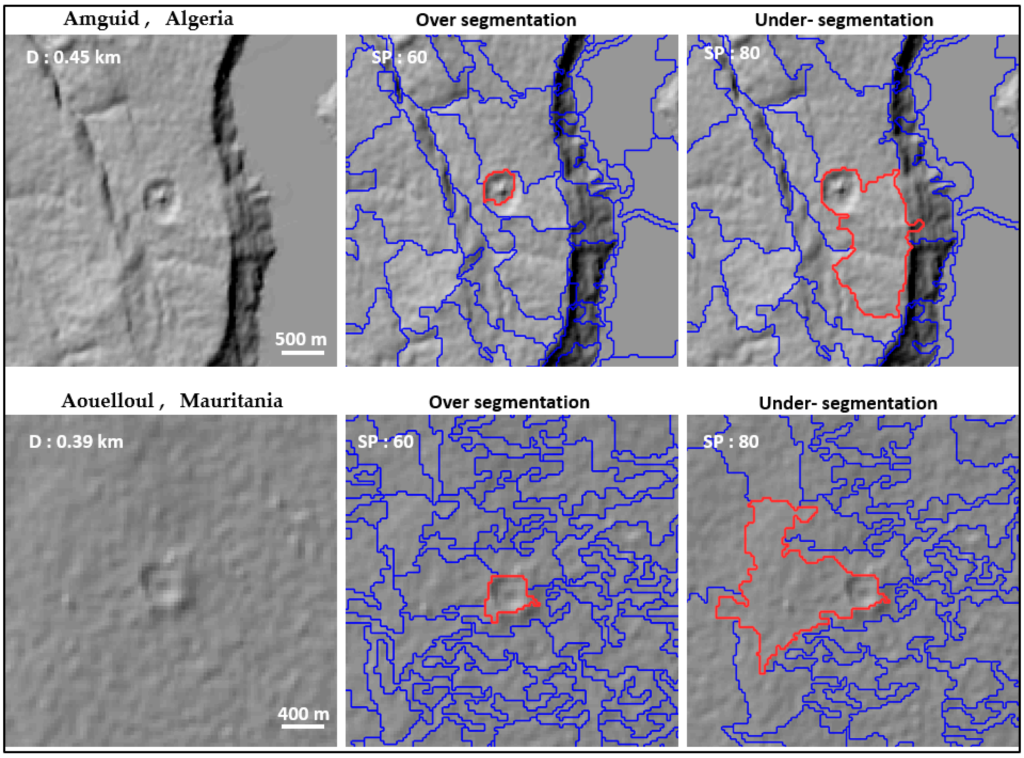

Figure A2. Representative segmentation of impact craters smaller than 0.88 km diameter showing unreliable segmentation results.

References

1. Bruzzone, L.; Lizzi, L.; Marchetti, P.G.; Earl, J.; Milnes, M. Recognition and detection of impact craters from EO products. *Eur. Sp. Agency Spec. Publ. ESA SP* **2004**, *553E.13B*, 85–92.
2. Ishak, B. *Encyclopedic Atlas of Terrestrial Impact Craters*; Contemporary Physics; Springer: Berlin/Heidelberg, Germany, 2019; Volume 60, p. 330, ISBN 9783030054496.
3. Grieve, R.A.F.; Therriault, A.M. Observations at terrestrial impact structures: Their utility in constraining crater formation. *Meteorit. Planet. Sci.* **2004**, *39*, 199–216. [CrossRef]
4. Kennedy, J.; Alanís, R.M. Book Review. *Carbohydr. Polym.* **2005**, *62*, 87. [CrossRef]
5. Schmieder, M.; Kring, D.A. Earth's Impact Events through Geologic Time: A List of Recommended Ages for Terrestrial Impact Structures and Deposits. *Astrobiology* **2020**, *20*, 91–141. [CrossRef]
6. Le Feuvre, M.; Wieczorek, M.A. Nonuniform cratering of the terrestrial planets. *Icarus* **2008**, *197*, 291–306. [CrossRef]

7. Kenkmann, T. The terrestrial impact crater record: A statistical analysis of morphologies, structures, ages, lithologies, and more. *Meteorit. Planet. Sci.* **2021**, *56*, 1024–1070. [CrossRef]
8. Crósta, A.P.; Reimold, W.U.; Vasconcelos, M.A.R.; Hauser, N.; Oliveira, G.J.G.; Maziviero, M.V.; Góes, A.M. Impact cratering: The South American record—Part 1. *Chem. Der Erde* **2019**, *79*, 1–61. [CrossRef]
9. Lobpries, T.A.; Lapen, T.J. Remote sensing evidence for a possible 10 kilometer in diameter impact structure in north-central Niger. *J. Afr. Earth Sci.* **2019**, *150*, 673–684. [CrossRef]
10. Reimold, W.U.; Koeberl, C. Impact structures in Africa: A review. *J. Afr. Earth Sci.* **2014**, *93*, 57–175. [CrossRef]
11. Wright, S.P.; Tornabene, L.L.; Ramsey, M.S. Remote Sensing of Impact Craters. *Impact Cratering Process. Prod.* **2012**, 194–210. [CrossRef]
12. Mansouri Daneshvar, M.R. Remote sensing analysis for the possible impact structure of Lakhčak Crater in southern Afghanistan. *Appl. Geomat.* **2015**, *7*, 275–282. [CrossRef]
13. Scholz, C.A.; Karp, T.; Lyons, R.P. Structure and morphology of the Bosumtwi impact structure from seismic reflection data. *Meteorit. Planet. Sci.* **2007**, *42*, 549–560. [CrossRef]
14. Vasconcelos, M.A.R.; Crósta, A.P.; Molina, E.C. Geophysical characteristics of four possible impact structures in the Parnaíba Basin, Brazil: Comparison and implications. *Spec. Pap. Geol. Soc. Am.* **2010**, *465*, 201–217. [CrossRef]
15. Theilen-Willige, B. Morphometric and Structural Evaluations of Satellite Data from the Bosumtwi Impact Structure and Adjacent Areas in Ashanti, Ghana. *Eur. J. Environ. Earth Sci.* **2021**, *2*, 7–14. [CrossRef]
16. Wang, X.Y.; Luo, L.; Guo, H.D.; Mu, L.L.; Li, C.; Ji, W.; Cai, H. Cratering process and morphological features of the Xiuyan impact crater in Northeast China. *Sci. China Earth Sci.* **2013**, *56*, 1629–1638. [CrossRef]
17. Crósta, A.P.; Kazzuo-Vieira, C.; Pitarello, L.; Koeberl, C.; Kenkmann, T. Geology and impact features of Vargeão Dome, southern Brazil. *Meteorit. Planet. Sci.* **2012**, *47*, 51–71. [CrossRef]
18. Maziviero, M.V.; Vasconcelos, M.A.R.; Crósta, A.P.; Góes, A.M.; Reimold, W.U.; De Carneiro, C. Geology and impact features of Riachão structure, northern Brazil. *Meteorit. Planet. Sci.* **2013**, *48*, 2044–2058. [CrossRef]
19. Williams, G.E.; Gostin, V.A. Geomorphology of the Acraman impact structure, Gawler Ranges, South Australia. *Cad. Do Lab. Xeol. Laxe* **2010**, *35*, 209–219.
20. Vamshi, G.T.; Martha, T.R.; Vinod Kumar, K. An object-based classification method for automatic detection of lunar impact craters from topographic data. *Adv. Sp. Res.* **2016**, *57*, 1978–1988. [CrossRef]
21. Sawabe, Y.; Matsunaga, T.; Rokugawa, S. Automated detection and classification of lunar craters using multiple approaches. *Adv. Sp. Res.* **2006**, *37*, 21–27. [CrossRef]
22. Urbach, E.R.; Stepinski, T.F. Automatic detection of sub-km craters in high resolution planetary images. *Planet. Space Sci.* **2009**, *57*, 880–887. [CrossRef]
23. Salamunićcar, G.; Lonarić, S.; Pina, P.; Bandeira, L.; Saraiva, J. MA130301GT catalogue of Martian impact craters and advanced evaluation of crater detection algorithms using diverse topography and image datasets. *Planet. Space Sci.* **2011**, *59*, 111–131. [CrossRef]
24. Masaitis, V.L. Morphological, structural and lithological records of terrestrial impacts: An overview. *Aust. J. Earth Sci.* **2005**, *52*, 509–528. [CrossRef]
25. Li, W.; Zhou, B.; Hsu, C.Y.; Li, Y.; Ren, F. Recognizing terrain features on terrestrial surface using a deep learning model—An example with crater detection. *Proc. 1st Work. GeoAI AI Deep Learn. Geogr. Knowl. Discov. GeoAI* **2017**, 33–36. [CrossRef]
26. Grieve, R.A.F. Economic natural resource deposits at terrestrial impact structures. *Geol. Soc. Spec. Publ.* **2005**, *248*, 1–29. [CrossRef]
27. Turtle, E.P.; Pierazzo, E.; Collins, G.S.; Osinski, G.R.; Melosh, H.J.; Morgan, J.V.; Reimold, W.U. Impact structures: What does crater diameter mean? *Spec. Pap. Geol. Soc. Am.* **2005**, *384*, 1–24. [CrossRef]
28. Osinski, G.R.; Silber, E.A.; Clayton, J.; Grieve, R.A.F.; Hansen, K.; Johnson, C.L.; Kalynn, J.; Tornabene, L.L. Transitional impact craters on the Moon: Insight into the effect of target lithology on the impact cratering process. *Meteorit. Planet. Sci.* **2019**, *54*, 573–591. [CrossRef]
29. Kenkmann, T.; Poelchau, M.H.; Wulf, G. Structural geology of impact craters. *J. Struct. Geol.* **2014**, *62*, 156–182. [CrossRef]
30. Holohan, E.P.; Schöpfer, M.P.J.; Walsh, J.J. Mechanical and geometric controls on the structural evolution of pit crater and caldera subsidence. *J. Geophys. Res. Solid Earth* **2011**, *116*, B07202. [CrossRef]
31. Geyer, A.; Martí, J. A short review of our current understanding of the development of ring faults during collapse caldera formation. *Front. Earth Sci.* **2014**, *2*, 22. [CrossRef]
32. Acocella, V. Regional and local tectonics at Erta Ale caldera, Afar (Ethiopia). *J. Struct. Geol.* **2006**, *28*, 1808–1820. [CrossRef]
33. Thouret, J.C. Volcanic geomorphology-an overview. *Earth Sci. Rev.* **1999**, *47*, 95–131. [CrossRef]
34. Carrión-Mero, P.; Montalván-Burbano, N.; Paz-Salas, N.; Morante-Carballo, F. Volcanic geomorphology: A review of worldwide research. *Geoscience* **2020**, *10*, 347. [CrossRef]
35. Straumann, R.K.; Purves, R.S. Delineation of valleys and valley floors. *Lect. Notes Comput. Sci. Incl. Subser. Lect. Notes Artif. Intell. Lect. Notes Bioinform.* **2008**, *5266*, 320–336. [CrossRef]
36. Bamber, E.R.; Goudge, T.A.; Fassett, C.I.; Osinski, G.R. Constraining the formation of paleolake inlet valleys across crater rims. *Icarus* **2022**, *378*, 114945. [CrossRef]
37. Survey USG. USGS [Internet]. Available online: https://earthexplorer.usgs.gov (accessed on 14 December 2021).
38. GVB-CSIC. CCDB [Internet]. Available online: https://gvb-csic.es/CCDB/ (accessed on 10 December 2021).

39. Trimble. *Trimble Documentation: eCognition® Developer User Guide*; Trimble Germany GmbH: Munich, Germany, 2018; pp. 1–272.
40. Drăguţ, L.; Eisank, C. Automated object-based classification of topography from SRTM data. *Geomorphology* **2012**, *141–142*, 21–33. [CrossRef]
41. Ma, L.; Li, M.; Ma, X.; Cheng, L.; Du, P.; Liu, Y. A review of supervised object-based land-cover image classification. *ISPRS J. Photogramm. Remote Sens.* **2017**, *130*, 277–293. [CrossRef]
42. Martha, T.R.; Kerle, N.; Jetten, V.; van Westen, C.J.; Kumar, K.V. Characterising spectral, spatial and morphometric properties of landslides for semi-automatic detection using object-oriented methods. *Geomorphology* **2010**, *116*, 24–36. [CrossRef]
43. Lucieer, A.; Stein, A. Existential uncertainty of spatial objects segmented from satellite sensor imagery. *IEEE Trans. Geosci. Remote Sens.* **2002**, *40*, 2518–2521. [CrossRef]
44. El-naggar, A.M. Determination of optimum segmentation parameter values for extracting building from remote sensing images. *Alex. Eng. J.* **2018**, *57*, 3089–3097. [CrossRef]
45. Yang, J.; He, Y.; Caspersen, J.; Jones, T. A discrepancy measure for segmentation evaluation from the perspective of object recognition. *ISPRS J. Photogramm. Remote Sens.* **2015**, *101*, 186–192. [CrossRef]
46. Li, P.; Song, B.; Guo, J.; Xiao, X. A Multilevel Hierarchical Image Segmentation Method for Urban Impervious Surface Mapping Using Very High Resolution Imagery. *IEEE J. Sel. Top. Appl. Earth Obs. Remote Sens.* **2011**, *4*, 103–116. [CrossRef]
47. DeFries, R.S.; Chan, J.C.W. Multiple criteria for evaluating machine learning algorithms for land cover classification from satellite data. *Remote Sens. Environ.* **2000**, *74*, 503–515. [CrossRef]
48. Castillejo-González, I.L.; Angueira, C.; García-Ferrer, A.; Orden, M.S. de la Combining object-based image analysis with topographic data for landform mapping: A case study in the semi-arid Chaco ecosystem, Argentina. *ISPRS Int. J. Geo.-Inf.* **2019**, *8*, 132. [CrossRef]
49. Olaya, V.; Conrad, O. *Geomorphometry in SAGA*; Elsevier: Amsterdam, The Netherlands, 2009; Volume 33, pp. 293–308, ISBN 9780123743459.
50. Van Den Eeckhaut, M.; Poesen, J.; Verstraeten, G.; Vanacker, V.; Moeyersons, J.; Nyssen, J.; van Beek, L.P.H. The effectiveness of hillshade maps and expert knowledge in mapping old deep-seated landslides. *Geomorphology* **2005**, *67*, 351–363. [CrossRef]
51. Wilson, J.P.; Gallant, J.C. (Eds.) *Terrain Analysis: Principles and Applications*; John Wiley & Sons: Hoboken, NJ, USA, 2000; p. 520. Available online: https://www.wiley.com/en-ie/Terrain+Analysis:+Principles+and+Applications-p-9780471321880 (accessed on 25 February 2022).
52. Na, J.; Ding, H.; Zhao, W.; Liu, K.; Tang, G.; Pfeifer, N. Object-based large-scale terrain classification combined with segmentation optimization and terrain features: A case study in China. *Trans. GIS* **2021**, *25*, 2939–2962. [CrossRef]
53. Takashimizu, Y.; Iiyoshi, M. New parameter of roundness R: Circularity corrected by aspect ratio. *Prog. Earth Planet. Sci.* **2016**, *3*, 2. [CrossRef]
54. Laliberte, A.S.; Rango, A. Texture and scale in object-based analysis of subdecimeter resolution unmanned aerial vehicle (UAV) imagery. *IEEE Trans. Geosci. Remote Sens.* **2009**, *47*, 761–770. [CrossRef]
55. Mason, B.G.; Pyle, D.M.; Oppenheimer, C. The size and frequency of the largest explosive eruptions on Earth. *Bull. Volcanol.* **2004**, *66*, 735–748. [CrossRef]
56. Tsikalas, F.; Faleide, J.I. Post-impact structural crater modification due to sediment loading: An overlooked process. *Meteorit. Planet. Sci.* **2007**, *42*, 2013–2029. [CrossRef]
57. Cole, J.W.; Milner, D.M.; Spinks, K.D. Calderas and caldera structures: A review. *Earth-Sci. Rev.* **2005**, *69*, 1–26. [CrossRef]
58. Mouginis-Mark, P.J.; Rowland, S.K. The geomorphology of planetary calderas. *Geomorphology* **2001**, *37*, 201–223. [CrossRef]
59. Krüger, T.; Hergarten, S.; Kenkmann, T. Deriving morphometric parameters and the simple-to-complex transition diameter from a high-resolution, global database of fresh lunar impact craters ($D \geq \sim 3$ km). *J. Geophys.Res. Planets* **2018**, *123*, 2667–2690. [CrossRef]
60. Schmincke, H. Cyclic caldera collapse: Piston or piecemeal subsidence? Field and experimental evidence. *Geology* **2002**, *30*, 135–138.
61. Lavallée, Y.; Stix, J.; Kennedy, B.; Richer, M.; Longpré, M.A. Caldera subsidence in areas of variable topographic relief: Results from analogue modeling. *J. Volcanol. Geotherm. Res.* **2004**, *129*, 219–236. [CrossRef]
62. McCall, G.J.H. Half a century of progress in research on terrestrial impact structures: A review. *Earth-Sci. Rev.* **2009**, *92*, 99–116. [CrossRef]